Journal of Applied Fluid Mechanics, Vol. 18, No. 10, pp. 2581-2598, 2025.
Available online at www.jafmonline.net, ISSN 1735-3572, EISSN 1735-3645.
https://doi.org/10.47176/jafm.18.10.3461

Hydrodynamic Characteristic and Prediction Study of 1, 1, 1, 2-Tetrafluoroethane under Supercritical Pressure

S. C. Liu[1,2,3], Z. G. Li[1,2,3†], W. Han[1,2], Y. X. Jiao[3], S. M. Zheng[4], X. T. Song[3], and J. H. Kou[4]

[1] *School of Energy and Power Engineering, Lanzhou University of Technology, Lanzhou 730050, China*
[2] *Key Laboratory of Advanced Pumps, Valves and Fluid Control System of the Ministry of Education, Lanzhou University of Technology, Lanzhou 730050, China*
[3] *Engineer school, Qinhai Institute of Technology, Xining 810016, China*
[4] *State Key Laboratory of Eco-hydraulics in Northwest Arid Region, Xi'an University of Technology, Xi'an 710048, China*

†Corresponding Author Email: lzhgui@mail.xhu.edu.cn

ABSTRACT

The supercritical organic Rankine cycle (S-ORC) is highly effective for utilizing medium- and low-temperature heat sources. This study investigated the hydrodynamic behavior of supercritical-pressure 1,1,1,2-tetrafluoroethane (R134a) within a horizontal 2 mm circular tube through integrated experimental and machine learning techniques. Experimental investigations spanned pressures between 4.2 and 5.4 MPa, inlet temperatures between 20 and 50 °C, and heat fluxes between 60 and 300 kW/m². Systematic analysis of hydrodynamic characteristics was accompanied by predictive modeling using an extreme learning machine (ELM) framework to forecast pressure drop trends. The hydrodynamic characteristic (HDC) curve of supercritical R134a exhibits significant differences from subcritical flow behavior—it lacks a negative-slope region but features a distinct "pressure drop stabilization region," where pressure drop remains consistent across a broad range of mass flow rates. The pressure-drop stabilization region diminishes with elevated system pressure or inlet temperature but enhanced with heat flux. Mechanistic analysis revealed that the initiation of this region is predominantly influenced by frictional pressure drop, whereas its termination correlates with acceleration pressure drop. Crucially, no flow instabilities were detected within the pressure-drop stabilization region. However, operation in the low-mass-flow-rate regime of the curve induced dynamic oscillatory behavior, characterized by periodic fluctuations in the mass flow rate, wall and fluid outlet temperatures, system pressure, and pressure drop. These instabilities are attributed to axial fluid density gradients arising from localized thermal nonequilibrium. The ELM model demonstrated robust predictive performance, maintaining errors within ±10% across all operating conditions, highlighting its effectiveness in analyzing supercritical hydrodynamic phenomena.

Article History

Received February 24, 2025
Revised May 11, 2025
Accepted May 30, 2025
Available online August 5, 2025

Keywords:

Hydrodynamic characteristics
Flow instability
Extreme learning machine
Supercritical R134a
Supercritical organic Rankine cycle

1. INTRODUCTION

The supercritical organic Rankine cycle (S-ORC) has emerged as a leading technology for low-grade energy recovery, owing to its superior thermal matching with heat sources and enhanced cycle efficiency. This technique is extensively employed in renewable energy systems, including solar, geothermal, and biomass energies, as well as in harnessing industrial waste heat (Cheng et al., 2021; Wang & Zhang, 2021; Ahmed et al., 2024; Shilpa & Mitul, 2024). Recent advances have highlighted the use of supercritical fluids as working mediums in the S-ORC system, leveraging their excellent thermal transport characteristics. This has shown promise in exploiting the advantages of the S-ORC, with the thermophysical properties of organic working fluids, such as R134a, which are fundamental to realizing this advantage (Astolfi et al., 2018; Li et al., 2023; Sobhan & Monjurul, 2023; Li et al., 2025). However, in S-ORC systems, the working fluid undergoes transcritical flow in the evaporator channels. Research indicates that near the pseudo-critical point, the properties of supercritical fluid exhibit significant

Nomenclature

c_p	specific heat	***Subscripts***	
G	mass flux	i	
m	mass flow rate	eff	
q	heat flux	b	
U	voltage	in	
I	current	out	
d	diameter	o	
L	length	w	
T	temperature	tot	
H	enthalpy	f	
z	distance between the local section	a	
$\overline{h}$	heat transfer coefficient	pc	
Nu	Nusselt number	sat	
Re	Reynolds number	SF	
U	voltage	SC	
p	pressure	cal	
Δp	pressure drop	exp	
h	specific enthalpy	***Superscripts***	
Greek symbols		*	
λ	thermal conductivity	***Abbreviation***	
μ	dynamic viscosity	S-ORC	
ρ	density	ELM	
η	thermal effectiveness	HDC	
β	isobaric thermal expansion coefficient	R134a	

nonlinear changes, which can easily induce flow instability during energy transfer (Valori et al., 2019; Pan et al., 2024). This instability affects the evaporator flow heat transfer efficiency and generates mechanical vibrations in the heat transfer equipment, thereby diminishing the operational stability of the system (Li et al., 2024; Luo et al., 2024; Wanstall et al., 2024, Zhou et al., 2025).

Flow instability phenomena are widely recognized in various thermodynamic systems that utilize fluids as the working media (Tracy et al., 2017; Li et al., 2023; Chen et al., 2024; Shi et al., 2024). Ledinegg (1938) made a pioneering contribution by investigating the multi-valued characteristics between the pressure drop and flow rate within heated pipelines—a phenomenon that is typically described by hydrodynamic characteristic (HDC) curves. Subsequently, numerous researchers have examined the HDC of fluids in two-phase flow systems. For instance, Nayak et al. (2022), Pandey and Singh (2017), Chen et al. (2018), and Cheng et al. (2018) conducted experimental investigations into the hydrodynamic characteristics of natural circulation loops. Additionally, Zhang et al. (2009) explored microchannels, while Jiang et al. (2024) and Yin et al. (2024) investigated the hydrodynamic characteristics of fluids in parallel channels. The results indicate that the HDC curves of fluids under subcritical pressure exhibit a distinct negative-slope region. When operating within the negative-slope region of the HDC curve, systems are prone to various types of flow instability phenomena, such as density-wave oscillations and pressure-drop instabilities. These instabilities result in a flow drift within the system, accompanied by fluctuations in both pressure and temperature (Li et al., 2022; Wang et al., 2022).

A divergence of opinion has been observed among researchers concerning the HDC of supercritical fluids. Some studies have suggested that the HDC curve of fluids at supercritical pressures do not exhibit a negative slope, Such as Swapnalee et al. (2012), Cai et al. (2021), and Singh and Chatoorgoon (2022) reported that supercritical CO_2 does not exhibit hydrodynamic multi-valued characteristics, with the pressure drop demonstrating a monotonic relationship with the mass flow rate. Conversely, studies by Ouyang et al. (2020), Liang et al. (2021), Guo et al. (2017), Yang and Shan (2018), and Chatoorgoon (2013) of supercritical water and supercritical hydrocarbon fuels indicate the presence of hydrodynamic multi-valued characteristics, with the characteristic curves demonstrating a clear negative slope. These studies further suggest that negative-slope region effectively suppressed with increasing system pressure. A study by Li et al. (2019) on the static flow instability of supercritical fluids in microchannels indicated that the negative-slope region in HDC curve is more pronounced in horizontal pipes than in vertical pipes. Some researchers have argued that although phase change does not occur in supercritical systems, a significant change in density in the high-heat-capacity region causes the fluid in the channel to experience a “pseudo-boiling” flow, akin to that of two-phase boiling flow. Consequently, supercritical fluids exhibit hydrodynamic characteristics analogous to those of two-phase flows during boiling. For example, Ambrosini (2007, 2011) first identified key dimensionless numbers in unstable two-phase flows, then extended this methodology to derive supercritical flow instability indicators. Mahmoudi (2009) further simplified the dimensionless parameters by comparing the flow instability of supercritical fluids and two-phase flow systems, inferring that the mechanisms of flow instability

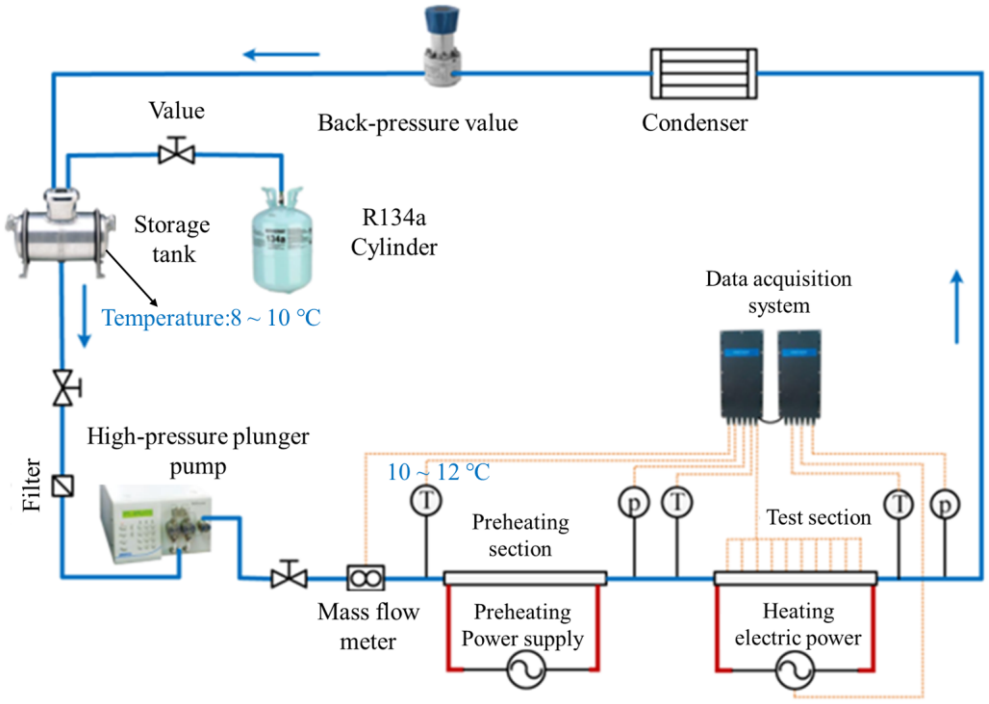

Fig. 1 Schematic of the experimental loop

in both systems are consistent. Building on this foundation, researchers have developed computational models for the hydrodynamic characteristics of supercritical fluids. Swapnalee et al. (2012) employed dimensionless parameter analysis and a linear approximation approach to describe the hydrodynamic characteristic curves of supercritical fluids, establishing an expression to forecast variations in fluid pressure drop. Farhadi (2009) developed a predictive model for the hydrodynamic characteristic curves of a two-phase flow in vertical pipes based on experimental findings and theoretical derivations. Nevertheless, these models predominantly rely on traditional equations and dimensional analysis, resulting in complex expressions that often lack practicality and universality, underscoring the need for further comprehensive scientific investigation.

In recent years, the accelerated advancement of artificial intelligence (AI) has facilitated the expanding adoption of machine learning (ML) techniques in multiphase flow and heat transfer research. (Sun et al., 2021; Manickathan et al., 2023; Zheng et al., 2024). Ma et al. (2021) established a backpropagation (BP) neural network model to effectively predict the heat transfer coefficient of supercritical water, achieving a standard deviation of only 4.13%. Similarly, Kuang et al. (2021), Bhanu et al. (2024), and Yu et al. (2024) employed an artificial neural network model to forecast the flow boiling heat transfer coefficient of saturated liquid hydrogen, resulting in an average absolute error of 12.2%. Yan et al. (2023) utilized a BP neural network to predict the heat transfer coefficient of supercritical R134a in heated channels, with over 90% of the data falling within ±5% accuracy range.

According to literature (Luo et al., 2024), the appearance of negative-slope regions in the HDC curves of supercritical fluids is critically influenced by the intrinsic properties of the working fluid. Moreover, the effects of relevant thermal parameters on the characteristic curves are inconsistent. Generally, elevating system pressure consistently eliminates the negative-slope region, while the effects of additional parameters (e.g., heat flux, subcooling degree) remain non-universal and require case-specific evaluation. Furthermore, computational models for HDC curves necessitate further investigation.

In this study, experimental research was conducted on the static and dynamic characteristics of R134a inside a 2 mm-diameter horizontal heated circular tube at supercritical pressures. The HDC curves of R134a under subcritical and supercritical pressures were obtained, and the effects of different thermodynamic parameters on the HDC curves of R134a at supercritical pressures were investigated. Additionally, advanced machine learning techniques were employed to predict the HDC curves. This study provides valuable insights for the effective design and optimization of evaporators in S-ORC systems.

2. Experiment Methods

2.1 Experimental System and Test Section

The experimental setup is illustrated in Fig. 1. Because of the low boiling point of R134a, it was thoroughly cooled prior to the experiment.

An insertion-type thermocouple was incorporated at the mid-height of the storage tank, and a K-type thermocouple was welded to the external bottom wall surface for real-time temperature monitoring. The R134a was considered to be in the liquid phase when the tank temperature reached 8–10 °C. Upon achieving complete phase transition to the liquid phase, it was transported into

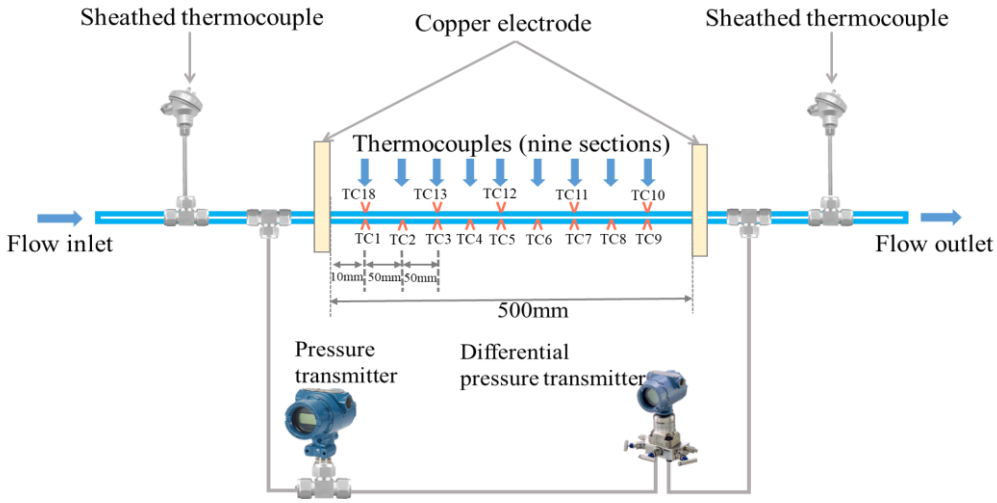

Fig. 2 Schematic of the test section

Table 1 Test conditions and measurement uncertainties

Parameter	Unit	Value	Uncertainties (%)
Mass flow rate	g/s	450–50	0.35
System pressure	MPa	4.2–5.4	0.30
Inlet temperature	°C	20–60	0.50
Heat flux	kW/m^2	60–300	3.50
Bulk temperature	°C	20–400	0.50

the primary circuit through a high-pressure plunger pump (Elitehplc, Model:1000+).

Subsequently, the working fluid was heated in the preheating section until it reached the predetermined experimental parameters before entering the test section. The high-temperature working fluid exiting the test section was cooled by a condenser. Following the pressure reduction by a backpressure valve, it flowed into the liquid storage tank, forming a closed-loop system. The liquid storage tank was equipped with internal water-cooled coils to enhance the cooling efficiency, and temperature-measuring thermocouples (Omega TJ2-CASS-M15U-250) were installed at the bottom of the tank to monitor the tank's real-time temperature and to determine the phase of R134a inside the tank.

A schematic of the test section is depicted in Fig. 2. The test section consisted of a 304 stainless steel (SS 304) circular tube with an inner diameter of 2 mm, a wall thickness of 0.5 mm, positioned horizontally, an effective heating length of 500 mm, and a length-to-diameter ratio of 250. The main loop of the test system utilized a 4 mm-inner diameter stainless steel circular tube to eliminate local disturbances caused by variable joints, and stabilizing sections of a specific length were incorporated at both ends of the inlet and outlet of the test section. Nine temperature measurement sections were arranged along the flow direction at 50 mm intervals on the bottom wall and at 100 mm intervals on the top wall. An alternating current electric heating method with low-voltage and high current was employed in the test section to generate a high heat flux. Furthermore, the test section was insulated with insulating cotton to reduce heat dissipation losses and ensure stable measurements of the outer-wall temperature.

2.2 Experimental Method and Test Accuracy

2.2.1 Experimental Method

Initially, the system flow rate was adjusted to a preset value (10 g/s), and then, the loop pressure was gradually adjusted to approach the predetermined experimental value using a backpressure valve. Subsequently, the power in the preheating section was gradually adjusted to elevate the fluid temperature to the predetermined value (the test section inlet temperature complied with the specified experimental parameters). At this stage, stabilization of the inlet and outlet temperatures of the test section must be ensured (outlet temperature variation: ≤1.0 °C, wall temperature variation: ≤1.0 °C). Subsequently, the heating power of the test section was adjusted to a preset value and maintained constant. The backpressure valve was gradually adjusted to achieve a stable loop pressure corresponding to the predetermined experimental value. Then, the loop flow rate was gradually reduced by adjusting the high-pressure constant-flow pump in steps of 10 mL/min. After each flow rate adjustment, real-time monitoring of the loop pressure was carried out, with minor adjustments to keep it constant at the preset experimental value. All parameters were allowed to stabilize (outlet temperature variation: ≤1.0 °C, wall temperature variation: ≤1.0 °C) before collecting data for 40–50 s. These steps were repeated until a set of operating conditions was tested.

HDC curves of supercritical R134a were obtained at different thermal parameters. The experimental conditions were designed using a controlled variable method; the specified test conditions are detailed in Table 1.

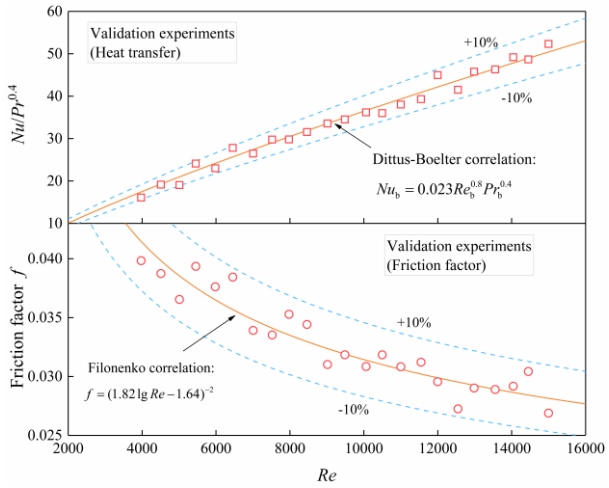

Fig. 3 Test bench calibration results

2.2.2 Test Accuracy and Reliability

In this study, the loop mass flow rate was measured using a Siemens MASS 2100 DI1.5 Coriolis mass flow meter with a range of 0–60 kg/h and an accuracy class of ±0.5%. The inlet and outlet fluid temperatures were recorded using Φ1.5 mm T-type sheathed thermocouples, featuring a measurement accuracy of ±0.4% and response time of less than 0.4 s. The outer wall temperature of the test section was measured using K-type thermocouples, covering a temperature range of 0–1300 °C, with an accuracy class of ±0.5%. The system pressure and test section pressure drop were measured using Rosemount and differential pressure transmitters, respectively. The pressure transmitter featured a measurement range of 0–27,000 kPa and an accuracy of ±0.05%, while the differential pressure transmitter had a range of 0–62 kPa and an accuracy of ±0.05%. The test section current was transmitted through a 200/5 A current transformer (accuracy: ±0.5%) to a current transmitter (accuracy: ±0.2%), which converted the measured alternating current signal into a linear direct current signal via a conversion module. The voltage of the test section was similarly measured using a voltage transmitter, with all data uniformly collected through an IMP acquisition board.

For indirectly measured values *Y*, which are functions of multiple directly measured quantities *Xi*, the relative uncertainty can be computed using the following expression:

$$\frac{\Delta Y}{Y} = \frac{1}{Y}\left[\sum_{i=1}^{N}\left(\frac{\partial Y}{\partial X}\right)^2\right]^{1/2} \quad (1)$$

The uncertainties of the parameters are outlined in Table 1. The measurement accuracy of the experimental setup was illustrated in Fig. 3. The majority of data points were within a ±10% error range, indicating that the measurement accuracy of the experimental setup meets the requirements.

For system reliability validation, 2-min experimental data segments were randomly selected for a comprehensive stability analysis. The analysis revealed the following: flow rate stability, ±0.03 g/s fluctuation amplitude (0.075% of mean value); outlet temperature variation, ≤1.0 °C; wall temperature variation, ≤1.0 °C; pressure stability, 10 kPa peak-to-peak fluctuation (0.22% of operating pressure). Considering the inherent pump pulsation characteristics, these fluctuations fall within an acceptable operational range.

2.3 Data Processing

The mass flux is calculated using Eq. (2).

$$G = \frac{4m}{\pi d_i^2} \quad (2)$$

The heat flux of the test section was calculated using Eq. (3).

$$q = \frac{UI\eta}{\pi d_i L_{eff}} \quad (3)$$

The thermal effectiveness was calculated using Eq. (4).

$$\eta = \frac{m(H_{b,o} - H_{b,i})}{UI} \quad (4)$$

In this study, the test section average thermal effectiveness was 90%.

The test section inner wall temperature $T_{w,i}$ was calculated by Eq. (5).

$$T_{w,i} = T_{w,o} - \frac{d_i}{2}\frac{q}{\lambda_w}\left[\frac{d_o^2}{d_o^2 - d_i^2}\ln\frac{d_o}{d_i} - \frac{1}{2}\right] \quad (5)$$

where λ_w is the thermal conductivity of the test section, which was composed of SS 304, with a thermal conductivity of 16.7 W/(m·K).

The bulk fluid enthalpy H_b was calculated from the inlet and outlet fluid enthalpies by linear interpolation using Eq. (6).

$$H_b = H_{b,i} + \frac{z}{L}(H_{b,o} - H_{b,i}) \quad (6)$$

The bulk temperature was calculated using the NIST REFPROP software corresponding to the bulk fluid enthalpy. The bulk flow temperature, defined as the average temperature within the measurement section, was calculated using Eq. (7).value of the measurement section temperature, calculated by:

$$T_b = \sum_{i=1}^{9} T_{b,i} \quad (7)$$

For horizontal pipelines, the gravitational pressure drop can be neglected. To ensure hydraulic flow development and eliminate entrance/exit effects, identical-diameter hydrodynamic stabilization sections were installed at the hydrodynamic development zones of both termini of the test section. Furthermore, the thermal isolation conduits flanking the test section were designed with a minimized length of 10 mm to ensure negligible frictional pressure drop of this region. Therefore, the measured total pressure drops across the test section exclusively comprised the frictional and accelerating pressure drops.

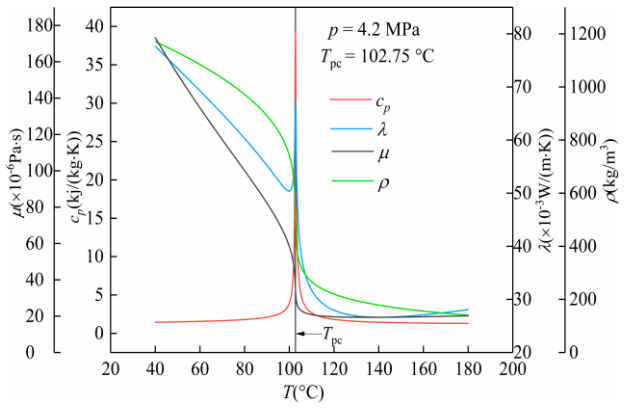

Fig. 4 Thermophysical properties of supercritical R134a

$$\Delta p_{tot} = \Delta p_f + \Delta p_a \tag{8}$$

Δp_a was calculated using Eq. (9).

$$\Delta p_a = G^2 \left(\frac{1}{\rho_{out}} - \frac{1}{\rho_{in}} \right) \tag{9}$$

where ρ_{in} and ρ_{out} are the inlet and outlet densities, respectively.

The heat transfer coefficient is calculated by:

$$\bar{h} = \frac{q}{T_{wi} - T_b} \tag{10}$$

The Nusselt number was calculated using Eq. (11).

$$Nu = \frac{\bar{h}L}{\lambda} \tag{11}$$

This section presents an in-depth overview of the experimental methods and data processing procedures employed in the study, particularly analyzing data reliability and measurement uncertainties, ensuring the reliability of the data.

3. RESULT AND DISCUSSION

3.1 Thermophysical Properties of Supercritical R134a

Figure 4 shows the variation in the thermophysical properties of R134a at supercritical pressure. The fluid specific heat capacity reaches its peak value at the pseudocritical temperature, with minimal variations in the specific heat at other regions. In contrast, the thermal conductivity declines sharply with increasing temperature but exhibits a rapid increase and a local peak at the pseudocritical temperature. Prior to reaching the pseudocritical temperature, the fluid viscosity drastically decreases with temperature, however, the trend of the viscosity change slows after surpassing the pseudocritical temperature. Additionally, the fluid density decreased significantly with increasing fluid temperature on both sides of the pseudocritical point. These drastic changes in the thermophysical properties significantly influence the fluid flow and heat transfer characteristics.

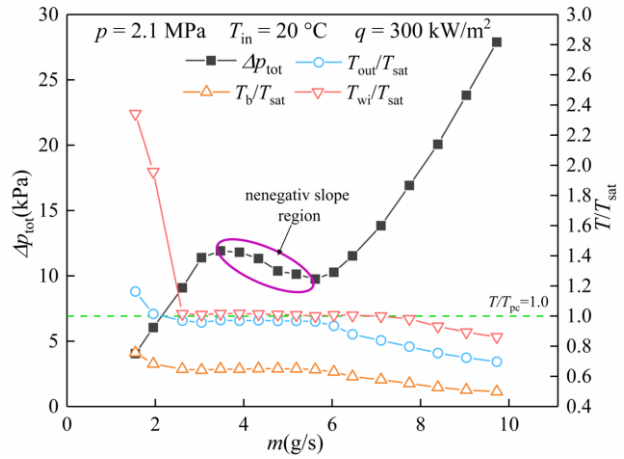

(a) Subcritical-pressure R134a

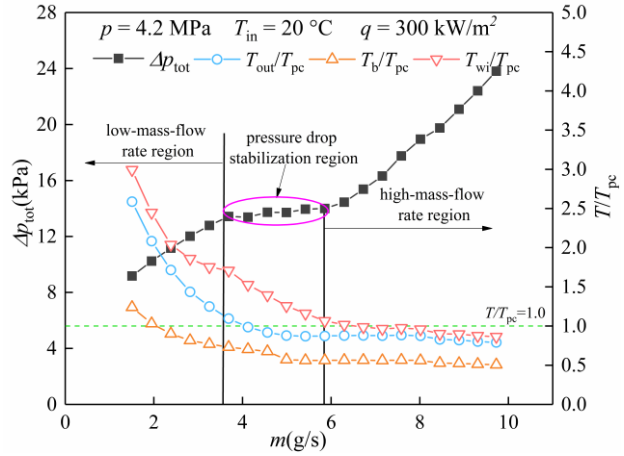

(b) Supercritical-pressure R134a

Fig. 5 HDC curves of R134a

3.2 Typical Hydrodynamic Characteristic Curve

Figure 5 illustrates the typical HDC curves of R134a at subcritical and supercritical pressures. As depicted in Fig. 5(a), the HDC curve of subcritical R134a features a negative-slope region. This region began where the wall temperature was higher than the boiling point temperature of the fluid, the bulk fluid temperature was significantly lower than the boiling point temperature, and the outlet temperature approached the boiling point temperature of the fluid. At this stage, the fluid within the channel is in a subcooled boiling state. Once the main flow undergoes complete boiling, the negative slope region vanishes, and the pressure drop changes revert to their original trends.

In contrast, the HDC curve of supercritical R134a (shown in Fig. 5(b)) does not exhibit a negative slope. When the wall temperature exceeds the pseudocritical temperature of the fluid, the outlet temperature remains slightly below the pseudo-critical temperature, and the bulk fluid temperature is substantially lower than the pseudo-critical temperature. The slope of the HDC curve approaches zero, indicating that the pressure drop within the channel exhibits minimum variation with changes in loop mass flow rate, thus reaching a relatively stable value. For the ease of further discussion and analysis, this study defines the region, characterized by this behavior as the

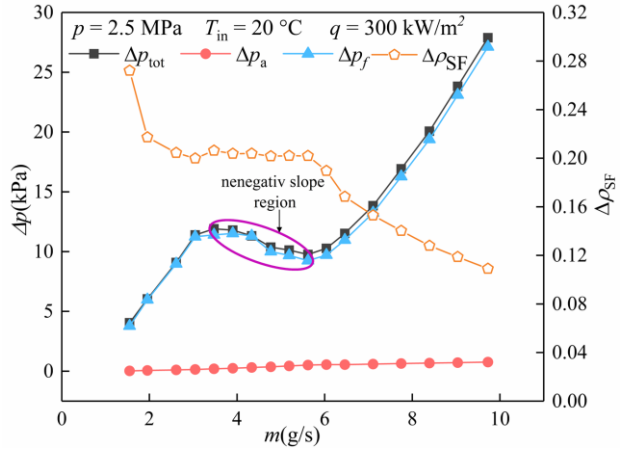

(a) Subcritical-pressure R134a

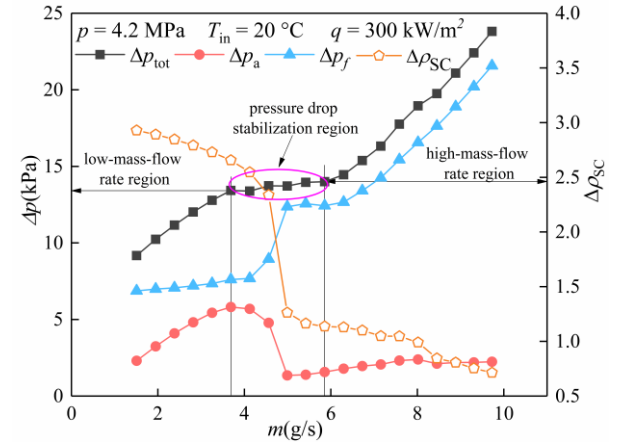

(b) Supercritical-pressure R134a

Fig. 6 Pressure drop and dimensionless density difference variation of R134a

"pressure drop stabilization region." This is because, at this point, regardless of the changes in mass flow rate, the pressure drop inside the channel remains relatively stable, suggesting a stable total pressure drop within the channel during this phase. Consequently, this area is defined as the pressure-drop stabilization region. When the fluid outlet temperature surpasses the pseudo-critical temperature, the "pressure drop stabilization region" concludes, and the system transitions into a low-mass-flow-rate region.

To further analyze the similarities and differences between the HDC curve of R134a under supercritical and subcritical pressure, two dimensionless parameters, $\Delta\rho_{SF}$ and $\Delta\rho_{SC}$, are defined as

$$\Delta\rho_{SF} = \frac{\rho_{in} - \rho_{out}}{\rho_{sat}} \tag{12}$$

$$\Delta\rho_{SC} = \frac{\rho_{in} - \rho_{out}}{\rho_{pc}} \tag{13}$$

where $\Delta\rho_{SF}$ represents the variations in the density difference between the inlet and outlet of the fluid under subcritical conditions relative to the density at the boiling point, while $\Delta\rho_{SC}$ represent density difference relative to the density at the pseudo-critical point under supercritical pressure conditions. These parameters were used to characterize the magnitude of the axial density difference in the fluid.

Figure 6 illustrates the changes in total pressure drop, frictional pressure drop, and accelerating pressure drop for R134a under both subcritical and supercritical pressure conditions, along with the variations in $\Delta\rho_{SF}$ and $\Delta\rho_{SC}$. In Fig. 6(a), the negative-slope region of the HDC curve for subcritical-pressure R134a is predominantly influenced by the frictional pressure drop of the fluid. This negative-slope region is situated where $\Delta\rho_{SF}$ remains relatively constant, indicating that phase change occurs within the fluid in the channel, causing $\Delta\rho_{SF}$ to remain unchanged.

Figure 6(b) indicates that the "pressure drop stabilization region" of the HDC curve for supercritical R134a is primarily governed by both frictional and accelerating pressure drops of the fluid. The onset of this region correlates with the frictional pressure drop of the fluid, while its endpoint is associated with the acceleration pressure drop of the fluid. This stabilization region is situated where the density difference between the inlet and outlet of the fluid reaches its maximum variation.

3.3 Parameter Effects

Figure 7 illustrates the HDC curves of the supercritical R134a under varying thermal parameters. Figure 7(a) depicts the effect of heat flux, Fig. 7(b) shows the impact of system pressure, and Fig. 7(c) illustrates the influence of inlet temperature. Notably, the HDC curve of supercritical R134a consistently exhibits a "pressure drop stabilization region" under varying parameters. The "pressure drop stabilization region" becomes more pronounced with an increase in heat flux; however, both an increase in system pressure and a rise in inlet temperature result in the disappearance of this region. Despite the onset of the "pressure drop stabilization region" shifting to a higher mass-flow rate area with the increasing heat flux and inlet temperature, it typically occurs when the outlet temperature is slightly below the pseudo-critical temperature ($T_{out} = 0.95\ T_{pc}$).

As mentioned previously, the HDC curves of supercritical R134a obtained in this study did not exhibit a negative-slope region, indicating the absence of static multiplicity. This finding is consistent with the results reported by Swapnalee et al. (2012) for supercritical CO_2.

Integrating findings from the systematic literature review with our experimental analysis, we propose that the hydrodynamic multiplicity of supercritical-pressure fluids is fundamentally associated with their thermophysical properties. Specifically, when the significant variation in fluid properties across the pseudo-critical temperature disrupts the local equilibrium between the frictional and accelerating pressure drops (i.e., when the change in the frictional pressure drop near the pseudo-critical point exceeds that of the accelerating pressure drop), the HDC curve manifests a negative-slope region. For fluids such as R134a and CO_2, under supercritical pressures, despite substantial variations in thermophysical properties near the pseudo-critical temperature, these changes may not reach the critical threshold required to trigger the occurrence of negative-slope regions in their HDC curves.

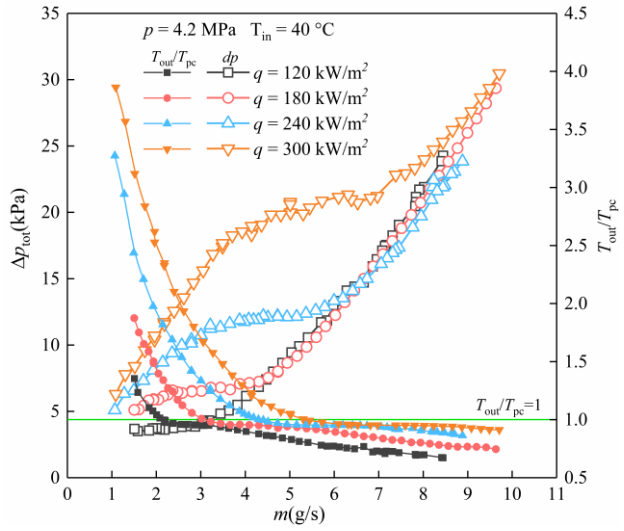

(a) Effect of heat flux

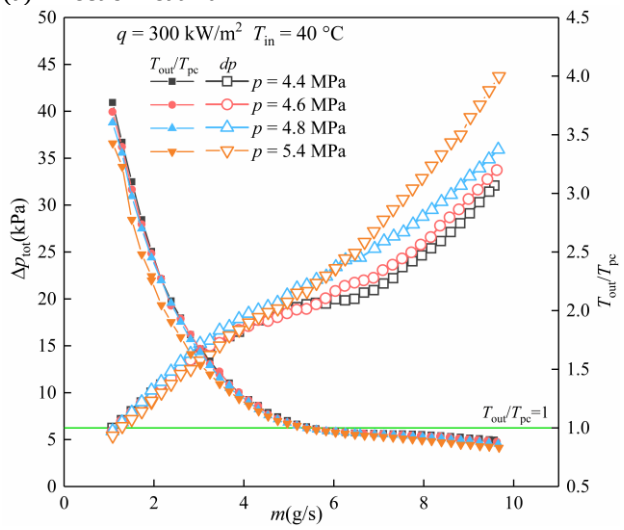

(b) Effect of system pressure

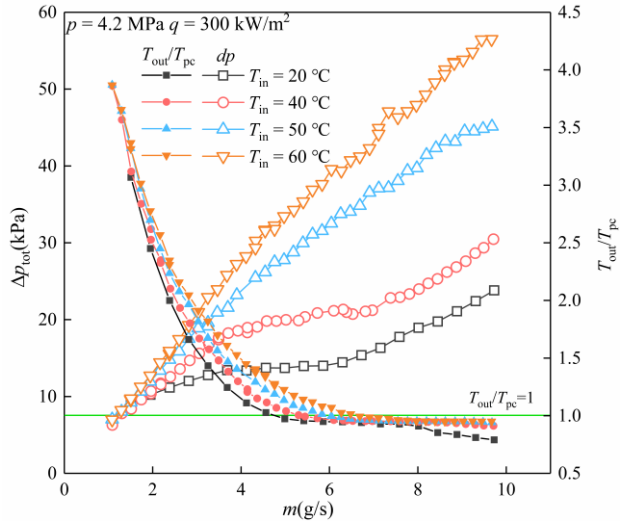

(c) Effect of inlet temperature

Fig. 7 Effect of thermal parameters on the HDC curve of supercritical-pressure R134a

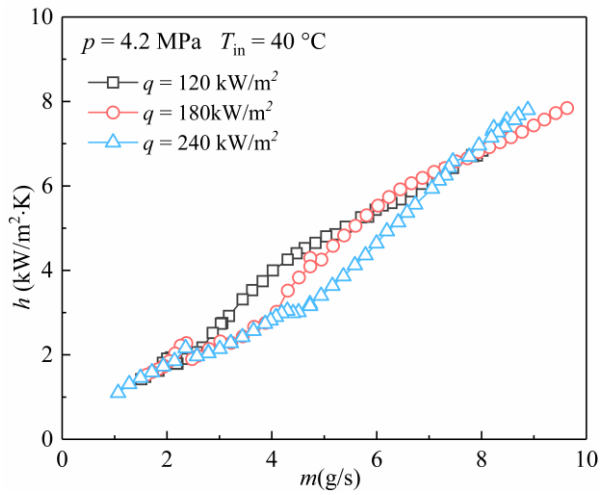

(a) Effect of heat flux

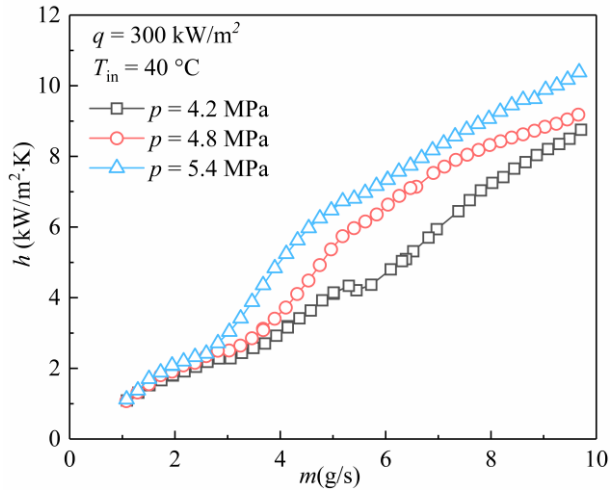

(b) Effect of system pressure

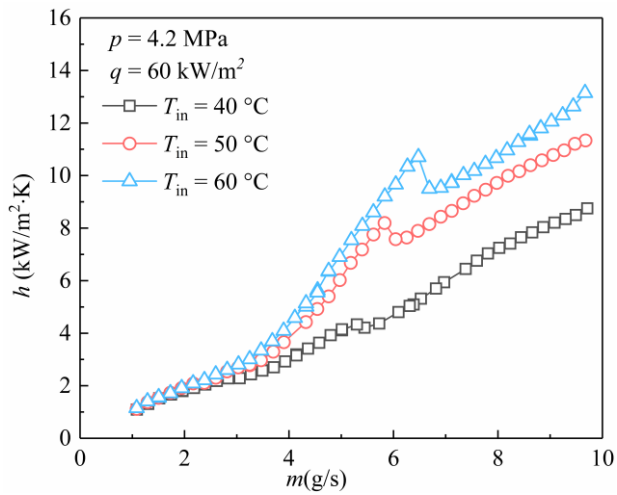

(c) Effect of inlet temperature

Fig. 8 Effect of thermal parameters on heat transfer of supercritical-pressure R134a

3.4 Heat Transfer Characteristics

Figure 8 depicts the variation in the heat transfer coefficient of the supercritical-pressure R134a with the loop mass flow rate for different thermal parameters. In the low-flow-rate regime, the effects of heat flux, system pressure, and inlet temperature on the heat transfer coefficient are marginal. This is because, at low mass flow rates, a high heat flux leads the fluid to enter the pipeline, with rapidly increasing temperature, and experience a significant decrease in density, and exhibit gas-like flow

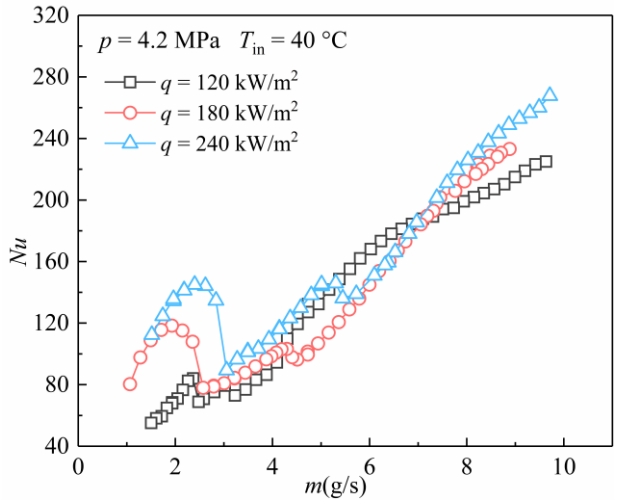

(a) Effect of heat flux

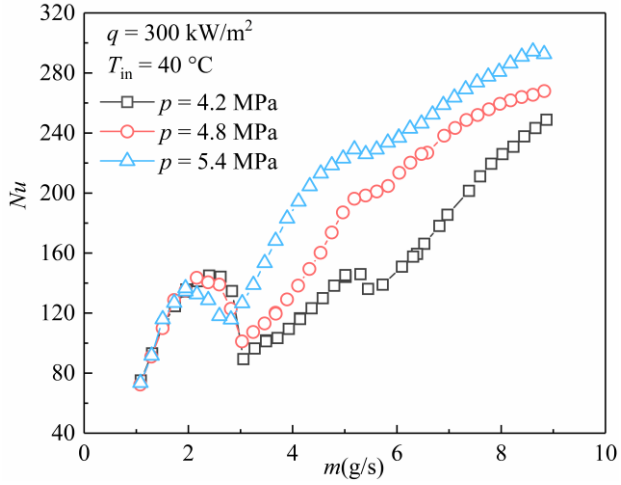

(b) Effect of system pressure

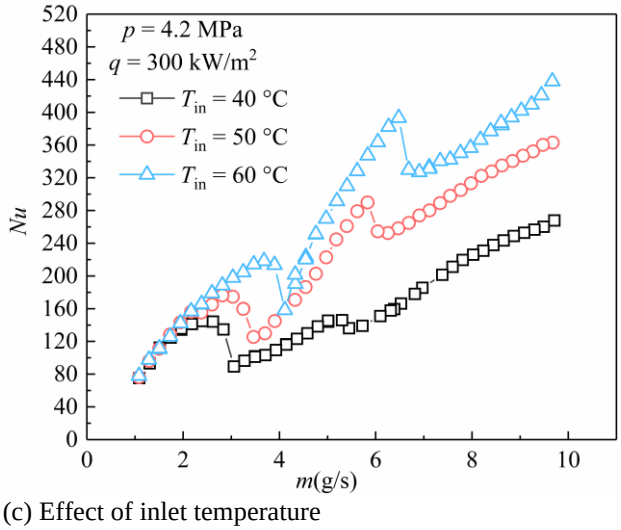

(c) Effect of inlet temperature

Fig. 9 Parametric effects on Nusselt number *(Nu)* characteristics

characteristics similar to a two-phase flow. Consequently, the fluid exhibits heat transfer characteristics resembling those of a gas.

Conversely, in the high-flow-rate regime, the heat transfer coefficient is augmented with the rise in the system pressure and inlet temperature. This is because the fluid properties are significantly influenced by the system pressure, and an increase in the inlet temperature leads to a reduction in the axial property difference of the fluid. This enhances the proportion of fluid within the large heat region of the pipe, thereby improving heat transfer performance.

Figure 9 shows the variation in the Nusselt number (*Nu*) for different thermal parameters. When the system operates with a mass flow rate surpassing 4 g/s, *Nu* rapidly diminishes with a reduced flow rate across all parameter conditions. As the flow rate approached and falls below 4 g/s, a local enhancement in *Nu* was observed before resuming its decreasing trend, indicating an elevated convective heat transfer capability of the fluid alongside diminished thermal resistance from the viscous sublayer.

A comparative analysis of Fig. 7 reveals that the flow rate corresponding to the local *Nu* peak closely aligns with the flow rate marking the termination of the pressure-drop stabilization region in HDC curve of R134a. This correlation further demonstrates that the emergence of the pressure-drop stabilization region is intrinsically linked to convective transport mechanisms and viscous boundary layer dynamics.

Figure 10 displays the axial wall temperature distribution patterns for various thermal-hydraulic parameters. The analysis revealed that the local temperature depression between Sections 4 and 6 becomes more pronounced with higher heat flux densities, lower system pressures, and reduced inlet temperatures. This phenomenon clearly indicates an enhanced convective heat transfer capacity at these cross-sections, leading to localized wall temperature reductions. Fluid temperature measurements confirmed that this region corresponded to the large-specific-heat zone flanking the pseudocritical point, where the combined effects of an increase in thermal conductivity and specific heat capacity synergistically intensified the heat transfer effectiveness.

3.5 Flow Instability Characteristics

The analysis revealed that the HDC curve of supercritical R134a did not exhibit a negative-slope region and did not display static multi-valued characteristics. However, experimental observations demonstrated that when the system operates in the low-flow-rate regime on its hydrodynamic characteristic curve, parameters such as the system pressure, loop flow rate, and pipe wall temperature fluctuate, leading to flow instability. Studies by Sørum et al. (2015), Park et al. (2018), O'Neill et al. (2018a, b), and Wang et al. (2022) regarding density wave instability flow suggest that this type of flow is particularly susceptible to oscillations in the low flow rate regime of the hydrodynamic characteristic curve, affecting parameters such as the loop flow rate, system pressure, test section pressure drop, and flow Reynolds number.

Figures 11 (a)–(d) illustrate the variations in the system parameters when the system operates under flow instability conditions. Analysis indicates that when the system flow rate decreases to 1.55 g/s, the loop flow rate begins to fluctuate, subsequently inducing fluctuations in fluid outlet temperature, pipe wall temperature, system pressure, and test section pressure drop. The mass-flow-rate fluctuation amplitude is 0.3 g/s, corresponding to 20%

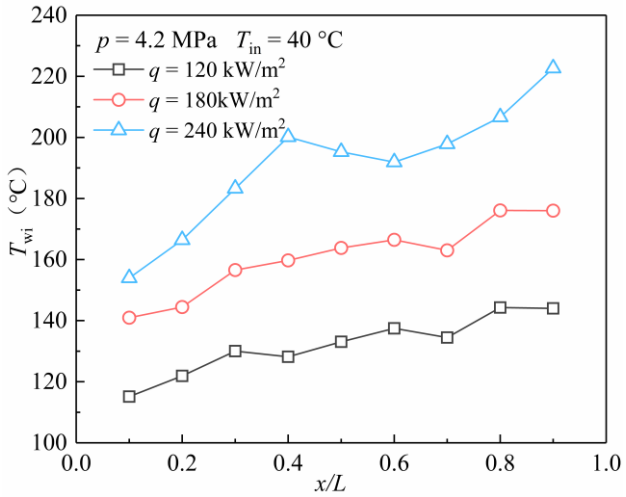

(a) Distribution under varying heat flux

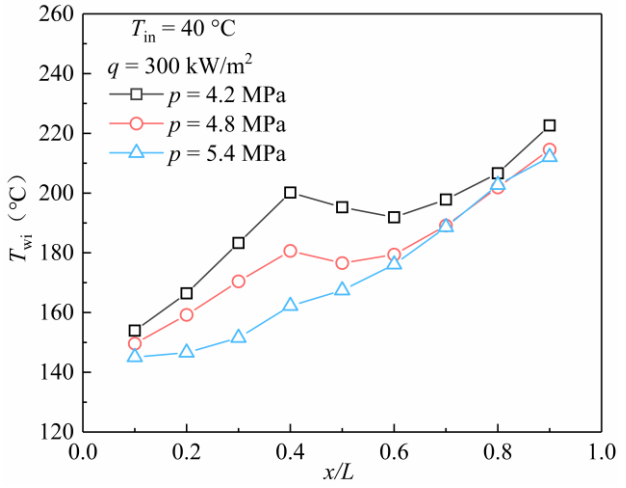

(b) Distribution under varying system pressure

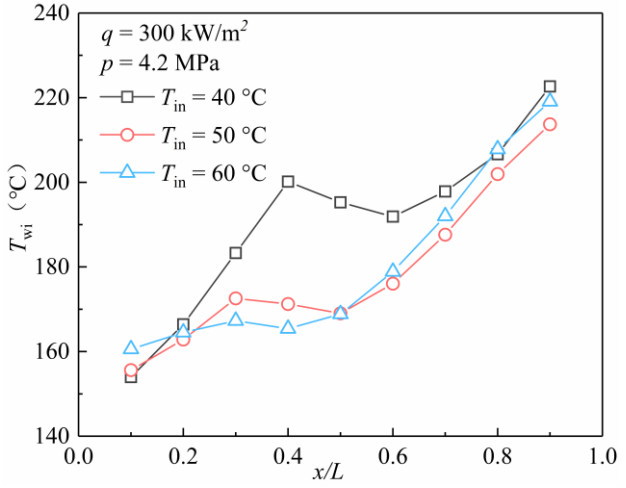

(c) Distribution under varying inlet temperature

Fig. 10 Axial wall temperature distribution under varying parameters

of the total loop flow rate, while the fluctuation in outlet temperature reaches up to 20 °C. The average outer-wall-temperature fluctuation amplitude is 23 °C, the system-pressure fluctuation amplitude is 150 kPa, and the test-section pressure drop fluctuation amplitude is 3 kPa, which accounts for 70% of the total pressure drop. Notably, the inlet-temperature fluctuation amplitude for the test section is 1 °C, signifying stability. (The inlet and outlet fluid temperatures were recorded using Φ1.5 mm T-type sheathed thermocouples, featuring a measurement accuracy of ±0.4%)

3.1 Flow Instability Mechanisms

Currently, two mechanisms are recognized for flow instability in supercritical fluids: viscosity variation and density collapse. Hines and Wolf (2012) proposed a viscosity variation mechanism to elucidate the formation of thermoacoustic oscillation-type instability in supercritical fluids. The authors stated that the cyclic feedback between "wall temperature–viscosity–boundary layer thickness–heat transfer coefficient" activates flow instability, resulting in oscillations of the parameters within pipelines.

Verdiev and Verdiev (2006) suggested that the significant density difference between the near-wall fluid and main flow is a critical factor inducing flow instability and parameter oscillations. Swapnalee et al. (2012) and Chatoorgoon (2013) further suggested that an abrupt change in fluid density is the primary cause of hydrodynamic multi-valued characteristics in supercritical fluids. Wang (2018, 2020) integrated these perspectives and attributed the dominant factors in the front and rear sections of heated pipes to viscosity and density mechanisms, respectively.

Currently, unified consensus is absent regarding the mechanisms of flow instability in supercritical fluids, and both the proposed density and viscosity mechanisms necessitate further validation.

Ambrosini (2011) proposed dimensionless expressions for density and enthalpy, which is suitable for supercritical fluid channels based on the similarity of fluid density variations in boiling two-phase flow and supercritical heating channels as follows:

$$h^* = \frac{\beta_{pc}}{C_{p,pc}}(h - h_{pc}) \tag{14}$$

$$\rho^* = \frac{\rho}{\rho_{pc}} \tag{15}$$

Therefore, we define dimensionless viscosity as follows:

$$\mu^* = \frac{\mu}{\mu_{pc}} \tag{16}$$

Figure 12 illustrates the changes in the test piece parameters along the axial section during flow instability under typical operational conditions. The inner wall temperature was significantly higher than the pseudocritical temperature. As the fluid approached the pseudocritical point, there was a rapid increase in the heat-transfer coefficient, leading to a reduction in the wall temperature. When the main flow temperature was either above or below the pseudo-critical point, the fluctuation in the bulk fluid temperature became more gradual, leading to a relatively stable heat-transfer coefficient, and subsequently maintaining a nearly constant wall temperature.

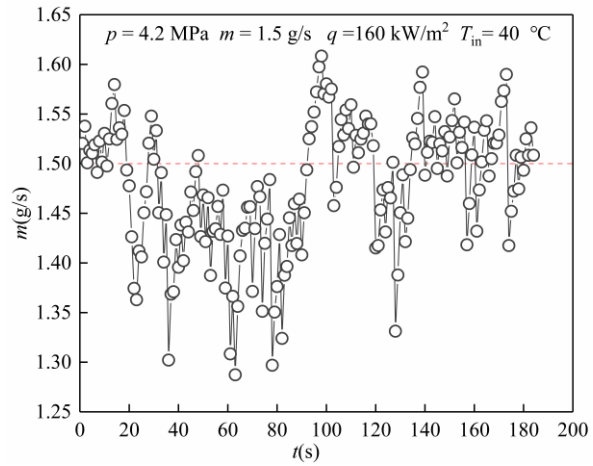

(a) Fluctuation in mass flow rate

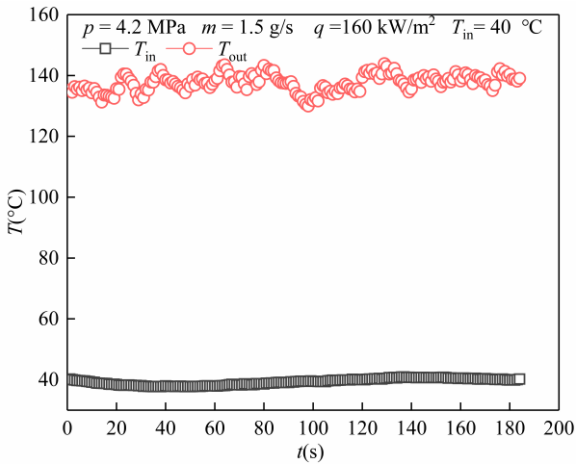

(b) Fluctuation in outlet temperature

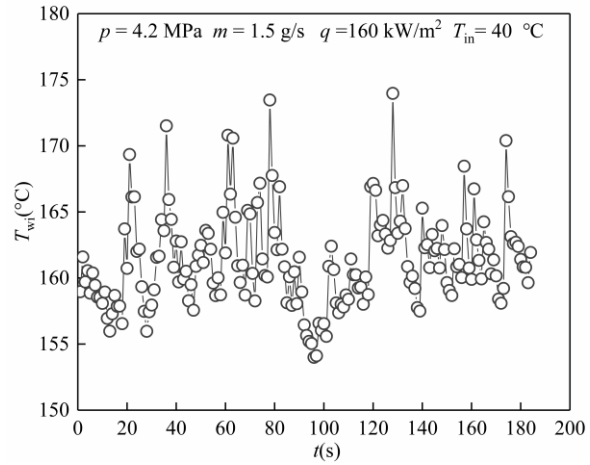

(c) Fluctuation in wall temperature

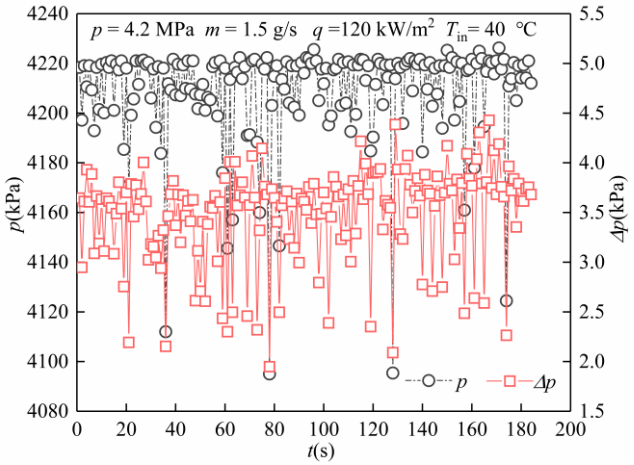

(d) Fluctuation in pressure and pressure difference

Fig. 11 Basic characteristics of flow instability at low-flow-rate region

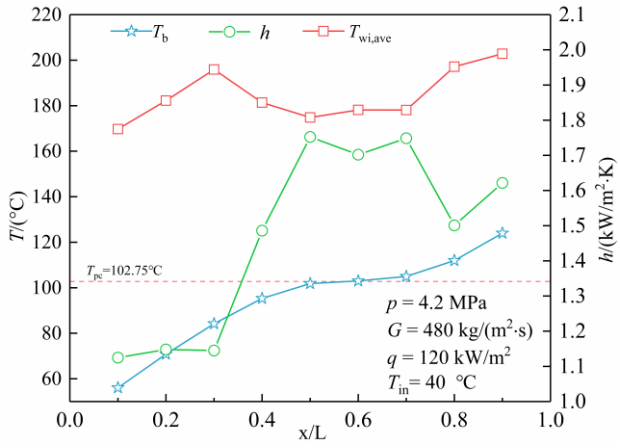

Fig. 12 Changes in axial section parameters

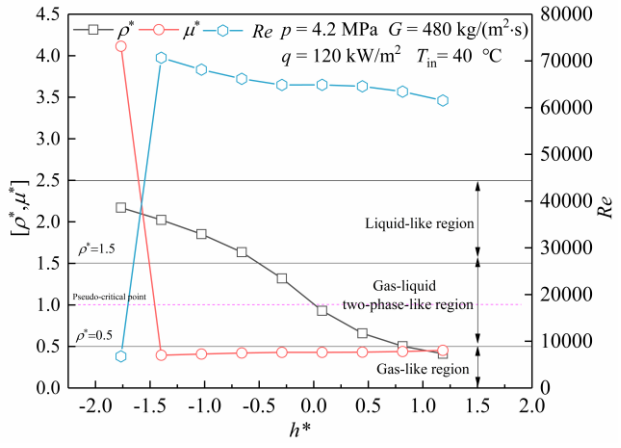

Fig. 13 No-dimensional parameter change

During this phase, the heat transfer behavior of the fluid was comparable to that observed in the boiling region.

Our previous study (Zhu et al., 2024) demonstrated that the flow can be categorized as liquid-like when the dimensionless density (ρ∗) is > 1.5. Conversely, the flow can be deemed gas-like when ρ∗ is < 0.5. For values within the range of 0.5 < ρ∗ < 1.5, the flow corresponds to a gas-liquid two-phase region. Figure 13 depicts the variations in the dimensionless parameters at each axial section under typical operational conditions during flow instability. Notably, minimal viscosity variations were observed in regions other than a significant shift in fluid

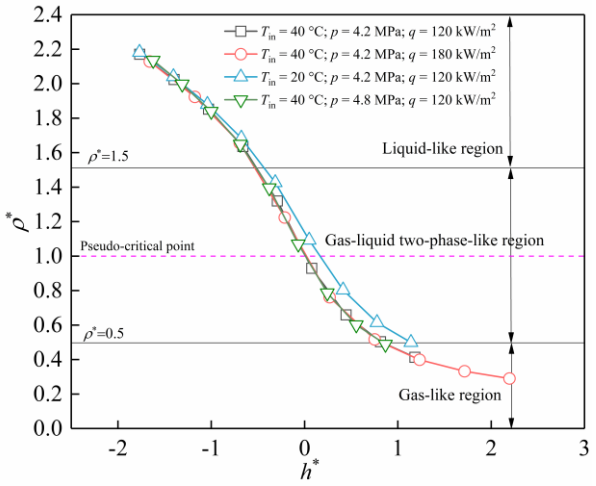

(a) Variation in dimensionless density

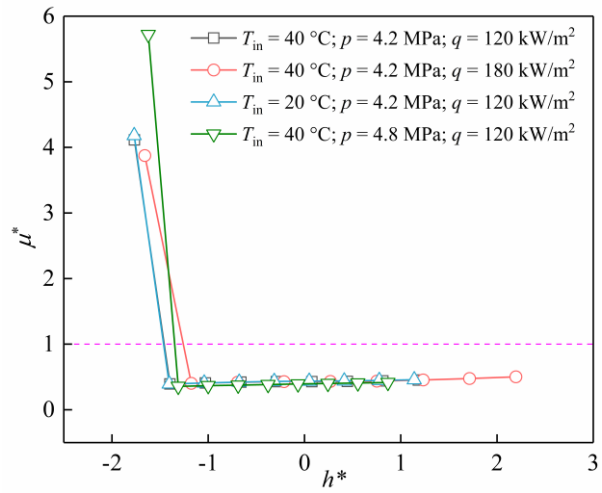

(b) Variation in dimensionless viscosity

Fig. 14 No-dimensional parameter changes under different working conditions

viscosity at the inlet. In contrast, the fluid density underwent substantial changes along the axial direction. The fluid within the pipeline transitions through distinct states, including liquid-like, vapor-liquid two-phase-like, and vapor-like flows.

Figure 14 depicts the variations in dimensionless viscosity and density under different operational conditions. Evidently, the fluctuations in the axial viscosity of the fluid are minimal across the various scenarios, whereas considerable changes in density are witnessed. Integrating this observation with the analysis described in Section 3.4, the flow inside the tube can be inferred to resemble the gas-phase flow characteristics associated with two-phase flow conditions owing to the combination of low mass flow rates and high wall heat flux. This behavior diminishes the influence of the thermal parameters on the heat transfer coefficient.

Consequently, when the bulk fluid, characterized by a higher density and lower temperature, enters the pipe at low flow rates with significant wall heat flux, the fluid density within the channel experiences a significant reduction. This leads to a rapid increase in the density differential between the inlet and outlet points over a very short duration, potentially causing substantial variation in density along a short axial distance near the channel entrance. Consequently, the channel becomes highly susceptible to flow instability conditions.

Based on a comprehensive analysis, the abrupt reduction in near-wall viscosity is found to activate boundary layer separation, providing an initial perturbation force for the onset of flow instability. Concurrently, the axial density gradient-induced "pseudo-boiling" phenomenon within the heated channel fundamentally sustains this flow instability.

The HDC of R134a were thoroughly investigated by analyzing its HDC curve. A comparative study of these curves under subcritical and supercritical pressures revealed that under supercritical conditions, the characteristic curve did not exhibit the negative-slope region (where the pressure drop increased with the flow rate reduced) observed under subcritical conditions. Instead, a relatively stable plateau region exists, where the pressure drop remains nearly constant despite the variations in flow rate. This plateau became more pronounced with an increase in the heat flux. The analysis of dimensionless parameters revealed that this shift in hydrodynamic behavior is primarily attributed to the competing effects of the frictional and acceleration pressure drops within the flow channel.

When the system operates in the low-flow-rate region of the hydrodynamic curve, density-wave instability occurs, leading to oscillations in the loop flow rate, fluid outlet temperature, pipe wall temperature, test section pressure difference, and system pressure. A mechanistic analysis confirmed that the primary cause of this instability was a significant axial density variation in the fluid.

4. PREDICTION ON HYDRODYNAMIC CHARACTERISTIC CURVE

4.1 Extreme Learning Machine Model

Based on the dimensionless density and enthalpy expressions provided by Ambrosini (2011), Swapnalee et al. (2012) employed a piecewise linear approximation method to evaluate the pressure drop of supercritical CO_2, summarized as follows:

The process of linear approximation for dimensionless density to establish a segmented region.

$$\rho^* = C_1 - C_2 h^* \tag{17}$$

Based on the piecewise-zoned approach, the Reynolds number (Re_{ss}) is defined distinctly for each characteristic region.

$$Re_{ss} = C\left[\frac{Gr_m^*}{N_G}\right]^r \tag{18}$$

The Reynolds numbers for the different zones were calculated using the above equations, followed by the determination of the frictional pressure drop in each zone

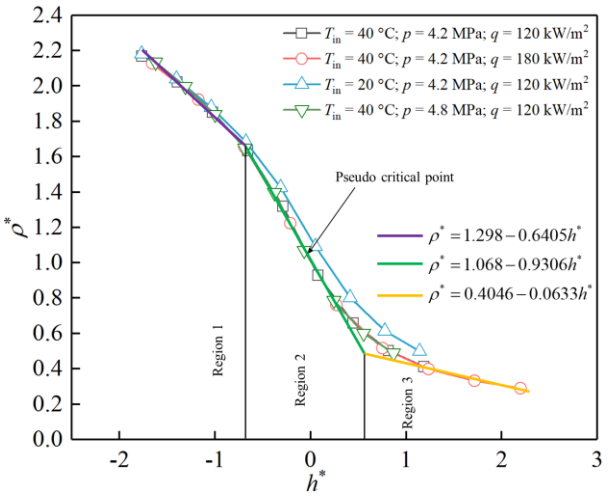

Fig. 15 Dimensionless density linear interpolation

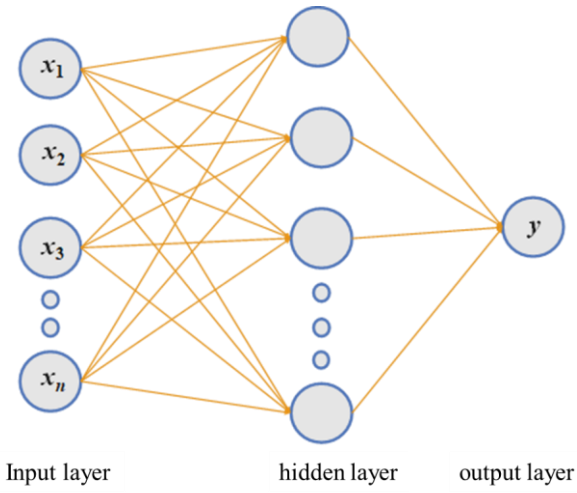

Fig. 16 Topological graph of Extreme Learning Machine

using the Blasius formula:

Among them, the parameters in Eq. (18) were calculated as follows:

$$Gr_m^* = \frac{D_r^3 \rho_{pc}^2 g \beta_{pc}^2 Q_h \Delta z}{A_r \mu^3} \tag{19}$$

$$N_G = \frac{L_t}{D_r} \tag{20}$$

$$C = \left(\frac{2C_2}{p} \right)^r \tag{21}$$

$$r = \left(\frac{1}{3-b} \right) \tag{22}$$

Based on Eq. (18–22), the dimensionless density under various test conditions is classified, and the results are illustrated in Fig. 15. Although this method demonstrates certain applicability, it fails to adequately capture the nonlinear characteristics of the dimensionless density within the h^* range of 0–1. Furthermore, the linear interpolation approach for the dimensionless density, proposed by Swapnalee et al. (2012), was developed using dimensionless density curves under various pressure conditions without accounting for the influence of the inlet temperature. As shown in Fig. 12 (for T_{in}=20 °C case), this method exhibits significant deviations when the inlet temperature varies. Consequently, this methodology not only involves complex and cumbersome pressure drop calculations but also leads to substantial errors across different operating conditions, restraining its effective application to specific scenarios.

In summary, the comprehensive analysis revealed that the existence of negative-slope regions in the HDC curves under supercritical pressure conditions is fundamentally dependent on the inherent properties of the working fluid. Moreover, the dimensionless density exhibits some variations under different thermal-hydraulic parameters, whereas the dimensionless parameters derived from conventional fluid dynamics equations demonstrate limited applicability across specific ranges. Consequently, the development of a universally applicable methodology that enhances predictive accuracy is imperative to characterize these complex phenomena more effectively.

With the advancement of artificial intelligence, machine learning algorithms leveraging big data have been gradually applied in the fields of fluid dynamics and heat transfer (Bhanu et al., 2024; Yu et al., 2024). An extreme learning machine (ELM) is a typical machine learning model (Huang et al., 2015), comprising an input layer, a hidden layer, and an output layer with interconnected weights between layers, as depicted in the Fig. 16.

The training process of the ELM model differs from that of traditional single-hidden-layer neural networks (e.g., BP neural networks). After generating the weights and thresholds for the input and hidden layers, the ELM model does not iterate using backpropagation but instead directly determines them at once by solving the pseudoinverse matrix. The ELM model significantly enhances the training speed while ensuring prediction accuracy, demonstrating strengths such as strong generalization, good robustness, and rapid training speed.

Based on an analysis of the factors influencing the dynamic characteristics of supercritical R134a, four parameters (mass flow rate, system pressure, inlet temperature, and heat flux) were selected as input variables to predict the pressure drop. The relationships among these parameters are as follows:

$$\Delta p = f(m, T_{in}, q, p) \tag{23}$$

To enhance the training speed and prediction accuracy of the prediction model, a preprocessing step was employed to normalize the prediction parameters and scale the data to the range of [0, 1]. The normalization formula is

$$Z' = \frac{Z - Z_{min}}{Z_{max} - Z_{min}} \tag{24}$$

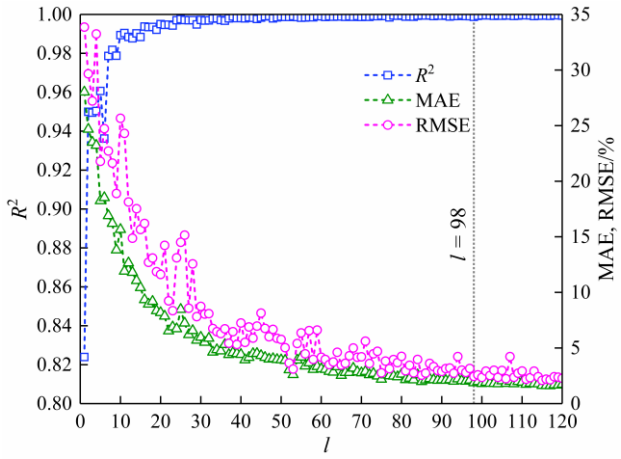

Fig. 17 Prediction performance of different neuron numbers in the hidden layer

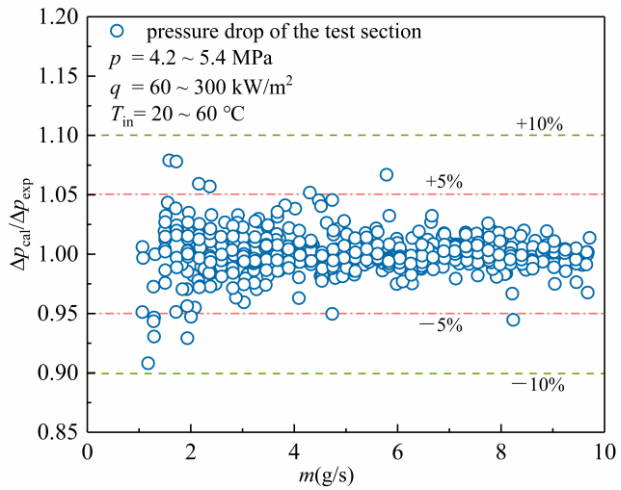

Fig. 18 Performance of the prediction model

4.2 Prediction Results

To prevent overfitting and reduce randomness, 498 sets of data were randomly divided into a training set (425 sets) and testing set (73 sets), at an approximate ratio of 8.5:1.5. The training set data were utilized to train the model, while the testing set data were exclusively used to validate the accuracy of the model. Furthermore, a search algorithm was implemented to determine the number of neurons in the hidden layer by comparing the regression coefficient R^2 of the testing set data with the mean absolute error (MAE) and root mean square error (RMSE) of all the experimental data.

$$\mathrm{MAE} = \frac{1}{N}\sum_{i=1}^{N}\frac{\left|\Delta p_{\mathrm{cal}}^2 - \Delta p_{\mathrm{exp}}^2\right|}{\Delta p_{\mathrm{exp}}^2}\times 100\% \tag{25}$$

$$\mathrm{RMSE} = \sqrt{\frac{1}{N}\sum_{i=1}^{N}\left(\frac{\Delta p_{\mathrm{cal}}^2 - \Delta p_{\mathrm{exp}}^2}{\Delta p_{\mathrm{exp}}^2}\right)^2}\times 100\% \tag{26}$$

where N represents the number of data points; Δp^2_{ca} and Δp^2_{exp} represent the predicted value and experimental value of the pressure difference Δp^2, respectively.

The search results, presented in Fig. 17, reveal that the predictive accuracy of the model gradually improves with an increase in the number of neurons. Notably, when $l \geq 85$, the model's predictive accuracy remains relatively stable. Moreover, when $l = 98$, the MAE and RMSE for all experimental data were remarkably low at 1.87% and 2.45%, respectively, whereas R^2 for the testing set data was as high as 0.9988. Considering that a further increase in the number of neurons will not only fail to enhance the predictive accuracy but also prolong the runtime, this study established that the number of neurons in the hidden layer was 98.

Figures 18 and 19 illustrate the prediction errors of the ELM model across all experimental data, as well as the model's performance under the operating conditions of system pressure p =4.2 MPa, T_{in} =40 °C, and q = 300 kW/m². The figures demonstrate that the ELM model provides high accuracy, with prediction errors for all data remaining within ±10%. In addition, the model accurately

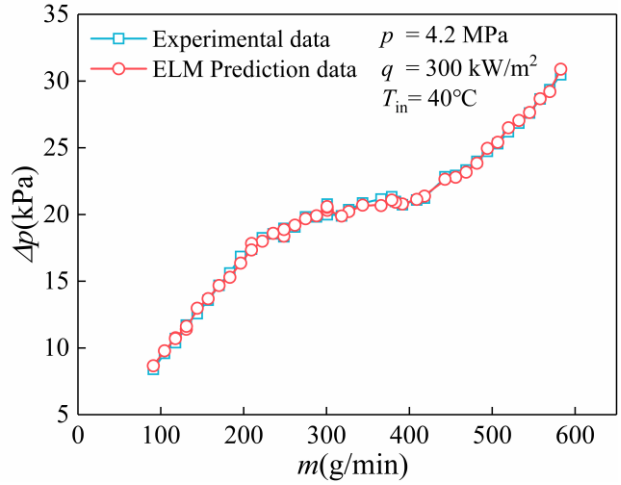

Fig. 19 Prediction performance under typical conditions

predicted the static characteristic curve of supercritical R134a. Therefore, the ELM exhibits excellent accuracy and generalization capability.

Based on the preceding analysis, this section elucidates the HDC of supercritical-pressure R134a in heated channels, presenting the predictive research using extreme machine learning methods. Compared to the piecewise linear interpolation approach documented in the literature for approximating the HDC curves of R134a, the extreme machine learning method demonstrated superior accuracy and applicability. These results substantiate that extreme machine learning is an effective methodology for investigating hydrodynamic behavior.

5. CONCLUSION

In this study, the experimental and predictive investigation into the HDC of R134a in a horizontally heated circular tube with an inner diameter of 2 mm has been carried out. The major conclusions are as follows.

(1) Subcritical R134a HDC curves exhibit a distinct negative slope region, which was primarily associated

with the occurrence of a boiling phase change within the tube. In contrast, supercritical R134a HDC curves do not exhibit such a negative-slope region; instead, a "pressure drop stabilization region" exists. The initiation of this zone was related to the frictional pressure drop, while its termination correlates with the fluid accelerating pressure drop. The significant change in fluid density on both sides of the pseudo-critical point, leads to the phenomenon of "pseudo-boiling," which is the primary reason for the existence of the "pressure drop stabilization region."

(2) When the system operates within the "pressure drop stabilization region" of the supercritical R134a HDC curve, it does not induce heat transfer and flow instability. However, operating in the low-mass-flow-rate region of the characteristic curve can induce flow instability, leading to fluctuations in the loop flow and consequently causing variations in the fluid outlet temperature, pipe wall temperature, system pressure, and pressure difference within the test section. A substantial change in the axial fluid density was the primary factor causing flow instability. The abrupt reduction in near-wall viscosity activated boundary layer separation, providing an initial perturbation force for the onset of flow instability.

(3) The influence of different thermal parameters on the HDC curve of supercritical R134a exhibited inconsistency. An ELM model was developed to predict the hydrodynamic characteristic curves of supercritical-pressure R134a. The prediction errors of the ELM model across all datasets were within ±10%, demonstrating its effectiveness in accurately predicting the HDC of supercritical R134a under various operating conditions.

ACKNOWLEDGEMENTS

The authors acknowledge financial support from the "Qinghai Kunlun Talent" Recruitment Scientific Research Project (2023-QLGKLYCZX-032). National Natural Science Foundation of China (52269022 and 52179086). Technology Research of Large-Scale Stepped Pumping Station Renovation of Jingtai River Electricity Irrigation Project (2020-70). The central government guides the local science and technology development fund projects (23ZYQA0320).

CONFLICT OF INTEREST

The authors have no conflicts to disclose.

AUTHORS CONTRIBUTION

Shouchun Liu: Writing-original draft, Investigation. **Zhenggui Li:** Conceptualization, Supervision, Writing review. **Wei Han:** Conceptualization, Supervision Proofread. **Yanxiong Jiao:** Investigation. **Shumin Zheng:** Formal analysis, Software. **Xiaotong Song:** Methodology. **Jiahao Kou:** Investigation.

REFERENCES

Ahmed, G., Peiwen, L., Abdel, L., & Babkir, A. (2024). Comparative techno-economic and environmental analysis of a relocatable solar power tower for low to medium temperature industrial process heat supply. *Energy*, *304*, 132085132085. https://doi.org/10.1016/j.energy.2024.132085

Ambrosini, W. (2007). On the analogies in the dynamic behaviour of heated channels with boiling and supercritical fluids. *Nuclear Engineering and Design*, *237*(11), 1164–1174. https://doi.org/10.1016/j.nucengdes.2007.01.006

Ambrosini, W. (2011). Assessment of flow stability boundaries in a heated channel with different fluids at supercritical pressure. *Annals of Nuclear Energy*, *38*(2), 615–627. https://doi.org/10.1016/j.anucene.2010.09.008

Astolfi, M., Alfani, D., Lasala, S., & Macchi E. (2018). Comparison between ORC and CO2 power systems for the exploitation of low-medium temperature heat sources. *Energy*, *161*, 1250–1261. https://doi.org/10.1016/j.energy.2018.07.099

Bhanu S. P., Chandan, K., Karthik K., Sriram D. K., Varun S. R., & Nagaraja, K. V. (2024). Investigation of the thermal analysis of a wavy fin with radiation impact: an application of extreme learning machine. *Physica Scripta*, *99*(1), 22. https://doi.org/10.1088/1402-4896/ad131f

Cai, D., Xu, X., Zhang, S., Liu, C., & Dang, C. (2021). Experimental investigation on the flow instability of supercritical CO2 in vertical upward circular tube in trans-critical CO2 Rankine system. *Applied Thermal Engineering*, *183*(P2), 116139. https://doi.org/10.1016/j.applthermaleng.2020.116139

Chatoorgoon, V. (2013). Non-dimensional parameters for static instability in supercritical heated channels. *International Journal of Heat and Mass Transfer*, *64*, 145–154. https://doi.org/10.1016/j.ijheatmasstransfer.2013.04.026

Chen, F., Zhang, J., Li, Z., Li, W., Yan, Z., & Liu, X. (2024). Effect of the surface coating of carbonyl iron particles on the dispersion stability of magnetorheological fluid. *Scientific Reports*, *14*(1), 11358. https://doi.org/10.1038/S41598-024-61934-2

Chen, X., Gao, P., Tan, S., Yu, Z., & Chen, C. (2018). An experimental investigation of flow boiling instability in a natural circulation loop. *International Journal of Heat and Mass Transfer*, *117*, 1125–1134. https://doi.org/10.1016/j.ijheatmasstransfer.2017.10.076

Cheng, C., Dai, Y., Yu, J., Liu, C., Wang, S., Feng, S., & Ni, M. (2021). Review of liquid-based systems to recover low-grade waste heat for electrical energy generation. *Energy & Fuels*, *35*(1), 161–175. https://doi.org/10.1021/acs.energyfuels.0c03733

Cheng, K., Meng, T., Tian, C., Yuan, H., & Tan, S. (2018). Experimental investigation on flow characteristics of pressure drop oscillations in a closed natural circulation loop. *International Journal of Heat and*

Mass Transfer, *122*, 1162–1171. https://doi.org/10.1016/j.ijheatmasstransfer.2018.02.030

Farhadi, K. (2009). A model for predicting static instability in two-phase flow systems. *Progress in Nuclear Energy*, *51*(8), 805–812. https://doi.org/10.1016/j.pnucene.2009.05.007

Guo, Y., Bi, Q., Liu, Z., Yang, Z., & Jiang, L. (2017). Experimental investigation on thermal-hydraulic characteristics of endothermic hydrocarbon fuel in 1mm and 2mm diameter mini-channels. *Applied Thermal Engineering*, *122*, 420–428. https://doi.org/10.1016/j.applthermaleng.2017.05.038

Hines, W. S., & Wolf, H. (2012). Pressure oscillations associated with heat transfer to hydrocarbon fluids at supercritical pressures and temperatures. *ARS Journal*, *32*(3), 361-366. https://doi.org/10.2514/8.6020

Huang, G., Huang, G. B., Song, S., & You, K. (2015). Trends in extreme learning machines: A review. *Neural Networks*, *61*, 32–48. https://doi.org/10.1016/j.neunet.2014.10.001

Jiang, J., Chen, C., Huang, H., & Pan, Z. (2024). Weakening of Ledinegg instability and maldistribution of boiling flow in parallel microchannels by entry effects. *Energies*, *17*(8), 1901. https://doi.org/10.3390/en17081901

Kuang, Y., Han, F., Sun, L., Zhuan, R., & Wang, W. (2021). Saturated hydrogen nucleate flow boiling heat transfer coefficients study based on artificial neural network. *International Journal of Heat and Mass Transfer*, *175*, 121406. https://doi.org/10.1016/j.ijheatmasstransfer.2021.121406

Ledinegg, M. (1938). Instability of flow during natural and forced circulation. *DieWärme*, *61*(89), 1–8.

Li, C., Fang, X., & Dai, Q. (2022). Two-phase flow boiling instabilities: A review. *Annals of Nuclear Energy*, *173*, 109099. https://doi.org/10.1016/j.anucene.2022.109099

Li, T., Yang, Z., & Zhang, B. (2019). Experimental study on flow instability onset coupling with heat transfer of supercritical fluid in mini-tubes. *Experimental Thermal and Fluid Science*, *109*, 109921. https://doi.org/10.1016/j.expthermflusci.2019.109921

Li, H., Zou, Z., Chen, Y., Du, P., Fu, C., & Wang, Y. (2023a). Experimental insights into thermal performance of a microtube precooler with drastic coolant properties variation and precooling impacts on turbojet engine operation. *Energy*, *278*(PA). https://doi.org/10.1016/J.ENERGY.2023.127916

Li, W., Li, Z., Han, W., Zhou J. (2023b). Measured viscosity characteristics of Fe3O4 ferrofluid in magnetic and thermal fields. *Physics of Fluids*, *35*(1), 012002. https://doi.org/10.1063/5.0131551

Li, W., Li, Z., & Han, W. (2024). Study of the flow characteristics of pumped media in the confined morphology of a ferrofluid pump with annular microscale constraints. *Journal of Fluids Engineering*, *147*(2), 021201. https://doi.org/10.1115/1.4066486

Li, W., Li, Z., & Han, W. (2023). Pumping-velocity variation mechanisms of a ferrofluid micropump and structural optimization for reflow inhibition. *Physics of Fluids*, *35*(5), 052005. https://doi.org/10.1063/5.0149130

Li, W., Li, Z., Han, W., Wang Y., Zhao J., Zhou J. (2025). Morphologic transformation of ferrofluid during micropump driving under field control. *Annals of the New York Academy of Sciences*, *1543*(1), 194–203. https://doi.org/10.1111/nyas.15261

Liang, Z., Xin, Y., Li, Y., Niu, T., & Yang, D. (2021). Experimental study on flow instability and oscillatory heat transfer characteristics of ultra-supercritical water in parallel channels. *International Journal of Heat and Mass Transfer*, *166*, 120754. https://doi.org/10.1016/j.ijheatmasstransfer.2020.120754

Luo, Q., Zhou, Y., Huang, J., Hu, W., Yuan, Y., & Huang, Y. (2024). A review of supercritical fluid flow instability. *Progress in Nuclear Energy*, *176*, 105376. https://doi.org/10.1016/j.pnucene.2024.105376

Ma, D., Zhou, T., Chen, J., Shi, Q., Muhammad, A., & Xiao, Z. (2017). Supercritical water heat transfer coefficient prediction analysis based on BP neural network. *Nuclear Engineering and Design*, *320*, 400–408. https://doi.org/10.1016/j.nucengdes.2017.06.013

Mahmoudi, M., Simchi, A., Milani, A. S. & Stroeve, P. (2009). Cell toxicity of superparamagnetic iron oxide nanoparticles. *Journal of Colloid and Interface Science*, *336*(2), 510-518.

Manickathan, L., Mucignat, C., & Lunati, I. (2023). A lightweight neural network designed for fluid velocimetry. *Experiments in Fluids*, *64*(10), 161. https://doi.org/10.1007/s00348-023-03695-8

Nayak, A. K., Kumar, N., Vijayan, P. K., Saha, D., & Sinha, R. K. (2022). Analytical study of flow instability behaviour in a boiling two-phase natural circulation loop under low quality conditions. *Kerntechnik*, *67*(2–3), 95–101. https://doi.org/10.1515/kern-2002-0042

O'Neill, L. E., Mudawar, I., & Hasan, M. M. (2018a). Experimental investigation into the impact of density wave oscillations on flow boiling system dynamic behavior and stability. *International Journal of Heat and Mass Transfer*, *120*, 144–166. https://doi.org/10.1016/j.ijheatmasstransfer.2017.12.011

O'Neill, L. E., Mudawar, I., & Hasan, M. M. (2018b). Experimental investigation of frequency and amplitude of density wave oscillations in vertical up

flow boiling. *International Journal of Heat and Mass Transfer*, *125*, 1240–1263. https://doi.org/10.1016/j.ijheatmasstransfer.2018.04.138

Ouyang, S., Niu, T., Dong, L., Zhou, X., & Yang X. (2020). Flow instability in parallel-channel systems with ultra-supercritical water. *International Communications in Heat and Mass Transfer*, *119*, 104907. https://doi.org/10.1016/j.icheatmasstransfer.2020.104907

Pan, Y., Zhai, Y., Wang, H., & Li, Z. (2024). Upstream heating history effects on heat transfer of supercritical R134a in transcritical organic Rankine cycle. *Energy* *309*, 133004. https://doi.org/10.1016/j.energy.2024.133004

Pandey, V., & Singh, S. (2017) Characterization of stability limits of Ledinegg instability and density wave oscillations for two-phase flow in natural circulation loops. *Chemical Engineering Science*, *168*, 204–224. https://doi.org/10.1016/j.ces.2017.04.041

Park, I., Fernandino, M., & Dorao, C. (2018). Experimental study on the characteristics of the pressure drop oscillations and their interaction with the short-period oscillation in a horizontal tube. *International Journal of Refrigeration*, *91*, 246–253. https://doi.org/10.1016/j.ijrefrig.2018.05.008

Shi, M., Duan, Z., Zhao, X., Wang, Z., Liu, S., & Xue, H. (2024). Experimental investigation on two-phase flow instability induced by direct contact condensation in open natural circulation. *Energy*, *292*, 130547. https://doi.org/10.1016/j.energy.2024.130547

Shilpa, V., & Mitul, L. (2024). Pressure drop measurements over anisotropic porous substrates in channel flow. *Experiments in Fluids*, *65*(9), 135–135. https://doi.org/10.1007/s00348-024-03873-2

Singh, I., & Chatoorgoon, V. (2020). Experiments and analyses of supercritical CO2 flow instability with study of wall heat-storage and dimensionless parameters. *Applied Thermal Engineering*, *186*(8), 116378. https://doi.org/10.1016/j.applthermaleng.2020.116378

Sobhan, C., & Monjurul, E. (2023). A critical overview of working fluids in organic Rankine, supercritical Rankine, and supercritical Brayton cycles under various heat grade sources. *International Journal of Thermofluids*, *20*, 100426. https://doi.org/10.1016/j.ijft.2023.100426

Sørum, M., & Dorao, C. A. (2015). Experimental study of the heat transfer coefficient deterioration during density wave oscillations. *Chemical Engineering Science*, *132*, 178–185. https://doi.org/10.1016/j.ces.2015.03.039

Sun, F., Xie, G., Song, J., Li, S., & Markides, C. (2021). Thermal characteristics of in-tube upward supercritical CO_2 flows and a new heat transfer prediction model based on artificial neural networks (ANN). *Applied Thermal Engineering*, *194*, 117067. https://doi.org/10.1016/j.applthermaleng.2021.117067

Swapnalee, B. T., Vijayan, P. K., & Sharma, M. (2012). Steady state flow and static instability of supercritical natural circulation loops. *Nuclear Engineering and Design*, *245*, 99–112. https://doi.org/10.1016/j.nucengdes.2012.01.002

Tracy, L., Mandel, I. R., Hayoon, C., Nicholas, T. O., & Jeffrey, R. K. (2017). Characterizing free-surface expressions of flow instabilities by tracking submerged features. *Experiments in Fluids*, *58*(11). 153. https://doi.org/10.1007/s00348-017-2435-6

Valori, V., Elsinga, E. G., & Rohde, M. (2019) Particle image velocimetry measurements of a thermally convective supercritical fluid. *Experiments in Fluids*, *60*(9), 1–14. https://doi.org/10.1007/s00348-019-2789-z

Verdiev, C. M., & Verdiev, D. C. (2006). Development of an improved mode of heat transfer of a hydrocarbon heat carrier under a supercritical pressure in an external acoustic field of a standing wave formed by thermoacoustic self-oscillations of pressure. *Heat Transfer Research*, *37*(3), 199-210. https://doi.org/10.1615/HeatTransRes.v37.i3.20

Wang, B., Hu, Y., He, Y., Rodionov, N., & Zhu, J. (2022). Dynamic instabilities of flow boiling in micro-channels: A review. *Applied Thermal Engineering* *214*, 118773. https://doi.org/10.1016/j.applthermaleng.2022.118773

Wang, X., & Zhang, M. (2021). The thermal Economy of a circulating medium and low temperature waste heat recovery system of industrial flue gas. *IJHT*, *39*(5), 1680–1688. https://doi.org/10.18280/ijht.390533

Wang, Y. H., & Li, S. F. (2020). Experimental investigation on thermoacoustic instability of supercritical-pressure aviation fuel. *Journal of Engineering Thermophysics*, *41*(8), 2025–2030. (in Chinese). https://doi.org/10.13675/j.cnki. tjjs.180474

Wang, Y. H., Li, S. F., & Zhao, X. H. (2018). Experimental study on flow instability of supercritical-pressure aviation kerosene. *Journal of Aerospace Power*, *33*(12), 2838–2844. (in Chinese). https://doi.org/10.13224/j.cnki.jasp.2018.12.003

Wanstal, T. C., Ferraiuolo, G., & Román, A. (2024). On the analysis of static thermal instabilities occurring in two-phase flow systems. *International Journal of Multiphase Flow*, *180*, 104975–104975. https://doi.org/10.1016/j.ijmultiphaseflow.2024.104975

Yan, J., Liu, S., Zheng, S., & Tian, H. (2023). Experimental study on heat-transfer performance of supercritical-pressure R134a and predictions based

on artificial neural network. *The Journal of Supercritical Fluids*, *192*, 105809. https://doi.org/10.1016/j.supflu.2022.105809

Yang, Z., & Shan, Y. (2018). Experimental study on the onset of flow instability in small horizontal tubes at supercritical pressures. *Applied Thermal Engineering*, *135*, 504–511. https://doi.org/10.1016/j.applthermaleng.2018.02.092

Yin, L., Wang, Y., & Jia, L. (2024) Flow boiling instability of R134a in the large-area heat sink with interconnected parallel multi-minichannels. *International Journal of Thermal Sciences*, *204*, 109193. https://doi.org/10.1016/j.ijthermalsci.2024.109193

Yu, C., Shao, M., Zhang, W., Huang, M., Wang, G. (2024). Enhancing heat transfer efficiency in corrugated tube heat exchangers: A comprehensive approach through structural optimization and field synergy analysis. *Heliyon*. *10*(9), e30113. https://doi.org/10.1016/j.heliyon.2024.e30113

Zhang, T., Tong, T., Chang, J., Peles, Y., Prasher, R., Jensen, M. K., & Phelan, P. (2009). Ledinegg instability in microchannels. *International Journal of Heat and Mass Transfer*, *52*(25/26), 5661–5674. https://doi.org/10.1016/j.ijheatmasstransfer.2009.09.008

Zheng, S., Yan, J., Wang, S., Wang, S., Liu, Z., & Zhu, F. (2024). Pressure drop for subcooled water boiling in microchannels under high heat fluxes: Experiments and predictions from artificial neural networks. *Applied Thermal Engineering*, *236*(PB), 121498. https://doi.org/10.1016/j.applthermaleng.2023.121498

Zhou, W., Jin, X., Ding, L., Lei, D., Ma, J., Su, H., & Zhao, A. (2025). Research on vibration signal decomposition of cracked rotor-bearing system with double-disk based on CEEMDAN-CWT. *Applied Acoustics*, *227*, 110254. https://doi.org/10.1016/j.apacoust.2024.110254

Zhu, X., Yan, J., Liu, S., & Zhu, F. (2024). Experimental investigation on hydrodynamic characteristics of 1,1,1,2-tetrafluoroethane (R134a) in a horizontal tube at supercritical pressures. *The Journal of Supercritical Fluids*, *204*, 106105. https://doi.org/10.1016/j.supflu.2023.106105